Research Article

Nano Research
2023, 16(10): 12286–12293

ISSN 1998-0124 CN 11-5974/O4
https://doi.org/10.1007/s12274-023-5904-7

Simultaneously enhanced interfacial shear strength and tensile strength of heterocyclic aramid fiber by graphene oxide

Ziyi Zhang[1,2,3], Xiangzheng Jia[4], Chun Li[3], Lanying Li[5], Yeye Wen[2], Zhenfei Gao[3], Jiangwei Zhang[6], Enlai Gao[4] (✉), Kun Jiao[2,3] (✉), and Jin Zhang[2,3] (✉)

[1] *College of Science, China University of Petroleum (Beijing), Beijing 102249, China*
[2] *Beijing National Laboratory for Molecular Sciences, School of Materials Science and Engineering, College of Chemistry and Molecular Engineering, Beijing Science and Engineering Center for Nanocarbons, Peking University, Beijing 100871, China*
[3] *Beijing Graphene Institute (BGI), Beijing 100095, China*
[4] *Department of Engineering Mechanics, School of Civil Engineering, Wuhan University, Wuhan 430072, China*
[5] *China Bluestar Chengrand Chemical Co., Ltd., Chengdu 610041, China*
[6] *Science Center of Energy Material and Chemistry, College of Chemistry and Chemical Engineering, Inner Mongolia University, Hohhot 010021, China*

Received: 31 March 2023 / **Revised:** 5 June 2023 / **Accepted:** 6 June 2023

ABSTRACT

Heterocyclic aramid fibers, a typical kind of high-performance fibers, have been widely used in aerospace and protection fields because of their excellent mechanical properties. However, the application of heterocyclic aramid fibers as a reinforcement is hindered by the weak interfacial combination with matrix materials, especially epoxy. Traditional strategies enhancing the interfacial shear strength (IFSS) usually decrease the tensile strength. Therefore, simultaneous enhancement of both mechanical properties remains a challenge. Herein, we report a novel heterocyclic aramid fiber with high interfacial shear strength (49.3 MPa) and tensile strength (6.27 GPa), in which 4,4′-diamino-2′-chlorobenzanilide (DABA-Cl) and a small amount of graphene oxide (GO) are introduced through *in-situ* polymerization. Hydrogen bonds and π–π interaction between GO and polymer chains trigger the enhancement in crystallinity, orientation, and lateral interaction of the fibers, thus improving the tensile strength and interfacial shear strength of the fibers. Moreover, the interfacial interaction between fiber and epoxy is enhanced due to the improvement of the surface polarity of the fibers caused by DABA-Cl. Therefore, a method to improve both tensile strength and interfacial shear strength of heterocyclic aramid fibers was found by introducing GO and DABA-Cl, which may provide guidance for the design and preparation of other high-performance fibers.

KEYWORDS

heterocyclic aramid fibers, graphene oxide (GO), 4,4′-diamino-2′-chlorobenzanilide (DABA-Cl), interfacial shear strength, tensile strength

1 Introduction

Heterocyclic aramid fibers (HAFs), a kind of high-performance organic fibers, show many excellent properties [1], such as low density, extraordinary mechanical properties, good chemical resistance, and heat resistance [2–5], and have been applied to aerospace, military, civil, and many other fields [6–10]. However, the application of high-performance fibers as reinforcing phases in advanced composite materials has been impeded by the weak interfacial combination between fibers and matrix [11]. The fundamental reason is that the surface of HAFs is smooth and chemically inert owing to their high crystallinity. Moreover, the skin–core structure of HAFs resulting from the wet spinning process can lead to the dominant failure of peeling of the skin–core layer or fibrillation, when HAFs are pulled out from epoxy. Therefore, in order to enhance the interfacial shear property of HAFs, the surface structures and the interaction between polymer chains should be taken into consideration [12–17].

Prior research has predominantly focused on improving the weak interfacial interaction between fibers and resins [11, 18, 19]. Based on physical and chemical surface modification of aramid fibers, such as high-energy radiation treatment [20–22], surface coating [23, 24], chemical grafting [25–27], and acid-base corrosion [28], numerous strategies were proposed to increase the polarity and roughness of the fiber surface and promote the formation of chemical bonding and mechanical interlocking between fibers and resins. However, such strategies caused defects on the skin and even in the core of the fibers, resulting in the deterioration of the tensile strength. For example, poly(catechol/polyamine) deposited onto the surface of aramid fibers via ultraviolet irradiation increased the adhesion force of aramid fibers to rubber by 67.5% but decreased the tensile strength by 11% [29]. Besides, another widely utilized method involves the chemical crosslink of polymer chains, which can improve the interfacial shear performance by enhancing the skin–core interaction through covalent bonds formed between polymer

Address correspondence to Enlai Gao, enlaigao@whu.edu.cn; Kun Jiao, jiaokun-cnc@pku.edu.cn; Jin Zhang, jinzhang@pku.edu.cn

chains. Notably, the chemical crosslink inevitably decreases the crystallinity and orientation of the fibers, leading to a decrease in tensile strength [30]. For example, by introducing a trace amount of oxygen to crosslink polymer chains, the interfacial shear strength (IFSS) of poly-(benzimidazole-terephthalamide) (PABI) fiber increased by nearly 28%, but the tensile strength dropped sharply [31].

Nowadays, it has become a focus to improve the interfacial shear property while ensuring the tensile strength of fibers. The introduction of nano-materials into polymers, which endows polymers with unique and improved properties, has aroused great interest among researchers [32–34]. Graphene is a two-dimensional (2D) material with outstanding mechanical properties, which has Young's modulus of nearly 1 TPa and tensile strength of 130 GPa in the plane and can be flexible in bending, twisting, and other deformation modes. Therefore, graphene is considered as an ideal composite reinforcement [35–40]. However, the van der Waals force between graphene and the polymer matrix is weak, resulting in a low load transfer efficiency. Compared with graphene, graphene oxide (GO) has many functional groups, such as epoxy, hydroxy, and carboxy groups, which help form strong interactions between fiber and matrixes, leading to efficient interfacial load transfer during mechanical deformation [41]. Meanwhile, GO has better dispersibility than graphene in most solvents due to the presence of polar functional groups [42–45]. Therefore, GO has unique advantages in the field of composite reinforcement.

Herein, we introduce 4,4′-diamino-2′-chlorobenzanilide (DABA-Cl) and GO into the polymerization process of HAFs, and the composite fiber (F3-Cl-GO) with high tensile strength and IFSS is prepared by wet spinning (Fig. 1(a)). The addition of the chlorine group and oxygen group increases the polarity of HAFs, thus improving the adhesive property between fibers and epoxy. GO is a 2D material with ultrahigh specific surface area, which can affect polymer chains in a few hundred nanometers in the radial direction and induces cracks deflection or elimination over a wide range, hindering the fiber failure caused by polymer chain slip. Interestingly, adding a small amount of GO provided additional hydrogen bonds and π–π interaction between polymer chains, which enhances the lateral interaction of the fibers and improve the crystalline orientation. Consequently, IFSS and the tensile strength of HAFs can be improved significantly. It is worth noting that the small addition of GO not only improved the mechanical properties of HAFs but also stained HAFs to a certain extent, which turned color from golden to brown (Fig. 1(b)). Moreover, the scanning electron microscopy (SEM) image and the transmission electron microscopy (TEM) image of the axial cross-section of F3-Cl-GO showed that GO was uniformly dispersed in F3-Cl-GO (Fig. 1(c)). As a result, the addition of DABA-Cl and GO helps increase the tensile strength and IFSS of F3-Cl-GO to 6.27 GPa and 49.3 MPa simultaneously. Compared with F3, the tensile strength and the IFSS were improved by 33.7% and 59.5%, respectively (Fig. 1(d)).

2 Experimental

2.1 Materials

Dimethylacetamide (DMAc, Macklin, ≥ 99%), lithium chloride (LiCl, Macklin, ≥ 99%), 5-(6)-amino-2-(4-amino-benzene)benzimidazole (PABZ, Macklin, ≥ 99%), DABA-Cl (Macklin, ≥ 99%), p-phenylenediamine (PPD, Macklin, ≥ 99%), terephthaloyl chloride (TPC, Macklin, ≥ 99%), dimethyl sulfoxide (DMSO, Macklin, ≥ 99%), GO (XFNANO, ≥ 98 wt.%), and potassium hydroxide (KOH, Macklin, ≥ 99%).

2.2 *In-situ* synthesis of F3, F3-Cl, and F3-Cl-GO spinning dope

GO powders were dispersed in DMAc solvent containing LiCl (3.5 wt.%). Then, the GO dispersion was ultrasonically treated for 0.5 h to obtain a uniform GO dispersion with a particle size of about 300 nm. PPD, PABZ, and DABA-Cl were added to the DMAc solution containing LiCl and stirred for 40 min until completely dissolved. Then the DMAc dispersion containing GO was added into the polymerization system. When the system temperature was cooled to below 10 °C, TPC was added in batches and stirred for 1.5 h. After the reaction was completed, F3-Cl-GO composite spinning dope with a viscosity of 50,000–60,000 cP was

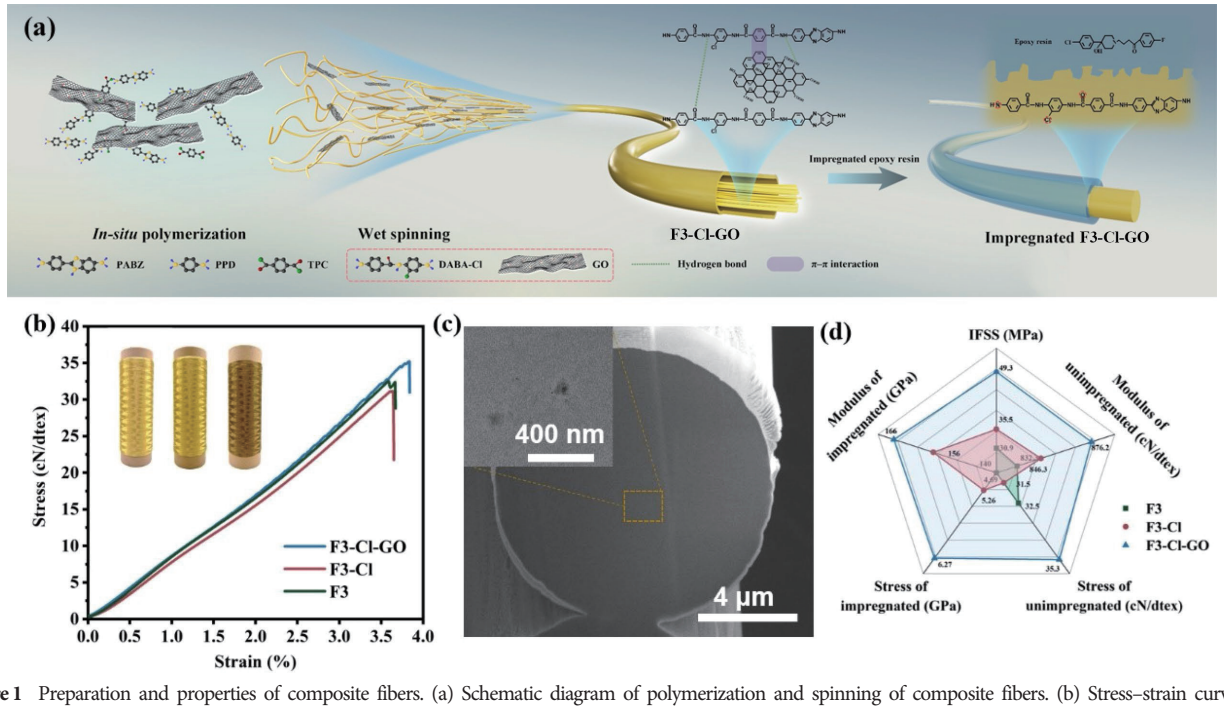

Figure 1 Preparation and properties of composite fibers. (a) Schematic diagram of polymerization and spinning of composite fibers. (b) Stress–strain curves of composite fibers and (inset) the digital photograph of F3, F3-Cl, and F3-Cl-GO from left to right. (c) SEM image and TEM image (inset) of the axial cross-section of F3-Cl-GO. (d) A radar plot revealing a comparison between the composite fibers.

obtained. The whole *in-situ* polymerization reaction was carried out in N_2 atmosphere. In the same way, F3-Cl spinning dope and F3 spinning dope were prepared without the addition of GO or GO and DABA-Cl.

2.3 Preparation of F3-Cl-GO fibers through wet spinning

F3-Cl-GO was obtained by wet spinning and heat treatment. After the spinning solution was treated by vacuum defoaming for 8 h in N_2 atmosphere, the spinning solution was extruded into a coagulation bath by a spinneret (300 holes with a diameter of 80 μm), and then successively passed through the two coagulation baths (50 wt.% DMAc and 50 wt.% H_2O, and 20 wt.% DMAc and 80 wt.% H_2O) under specific stretching ratios. Subsequently, the fibers were washed with water to remove residue DMAc and HCl. The obtained primary fibers were dried, then subjected to a thermal stretching treatment in N_2 atmosphere at 400 °C. Finally, the F3-Cl-GO was collected by winding.

2.4 Characterization

The morphology of the axial cross-section of the fibers was observed by TEM. The surface morphology of the fibers was observed by SEM. The 2D-wide-angle X-ray diffraction (WAXD) patterns were obtained by X-ray diffractometer on a beam line (BL17B) at Shanghai Synchrotron Radiation Facility. Small-angle X-ray scattering (SAXS) experiments were performed on a beam line (BL19U2) at Shanghai Synchrotron Radiation Facility. X-ray photoelectron spectroscopy (XPS) spectra of all samples were obtained on an X-ray photoelectron spectrometer (X-Pert3 Powder). Fourier transform infrared (FTIR) spectrometer (Nicolet iS50) and attenuated total reflection attachment were used to analyze the functional groups of GO and the fibers with the range of 4000–400 cm^{-1}. The dispersibility of GO was measured by ultraviolet–visible-near infrared (UV–vis–NIR) spectrometer (UV, Perkin Elmer Lambda 950). The Raman spectra were analyzed by LabRAM HR Evolution with a 532 nm laser. The roughness of the fibers surface was measured by atomic force microscopy (AFM), and the scanning area was 4 μm × 4 μm. The particle size of GO dispersed in water was measured by particle size analyzer (BLUEWAVE S3500). The tensile strength of the fibers was measured on electromechanical universal testing machine (CMT6103) instrument. The strain rate was controlled at 25 mm·min^{-1} and the gauge length was 170 mm. The performance of IFSS was obtained by a nano-mechanical testing system (LLQ-T150, Agilent T150).

3 Results and discussion

3.1 Characterization of GO and GO dispersion

As an important additive, the structure and morphology of GO were investigated. The XPS C 1s spectrum of GO can be deconvolved into four components (Fig. 2(a)), which are C=C (284.8 eV), C–O (286.5 eV), C=O (288.8 eV), and O–C=O (290.7 eV) [46], respectively. This means that the surface of GO contains functional groups such as –OH, –COOH, and C–O–C. The survey scan spectrum of XPS showed that the atom ratio of O to C (O/C) reached 35%. The abundant oxygen-containing functional groups bring many advantages. Firstly, they are conducive to the dispersion of GO in the polymerization system. Secondly, they can form hydrogen bonds between polymer chains and GO, preventing slipping between the polymer chains in the interfacial region and enhancing the polarity of the fiber surface. Raman spectrum (Fig. 2(b)) show two specific peaks located at 1332 cm^{-1} (D band) and 1580 cm^{-1} (G band), which reflect the

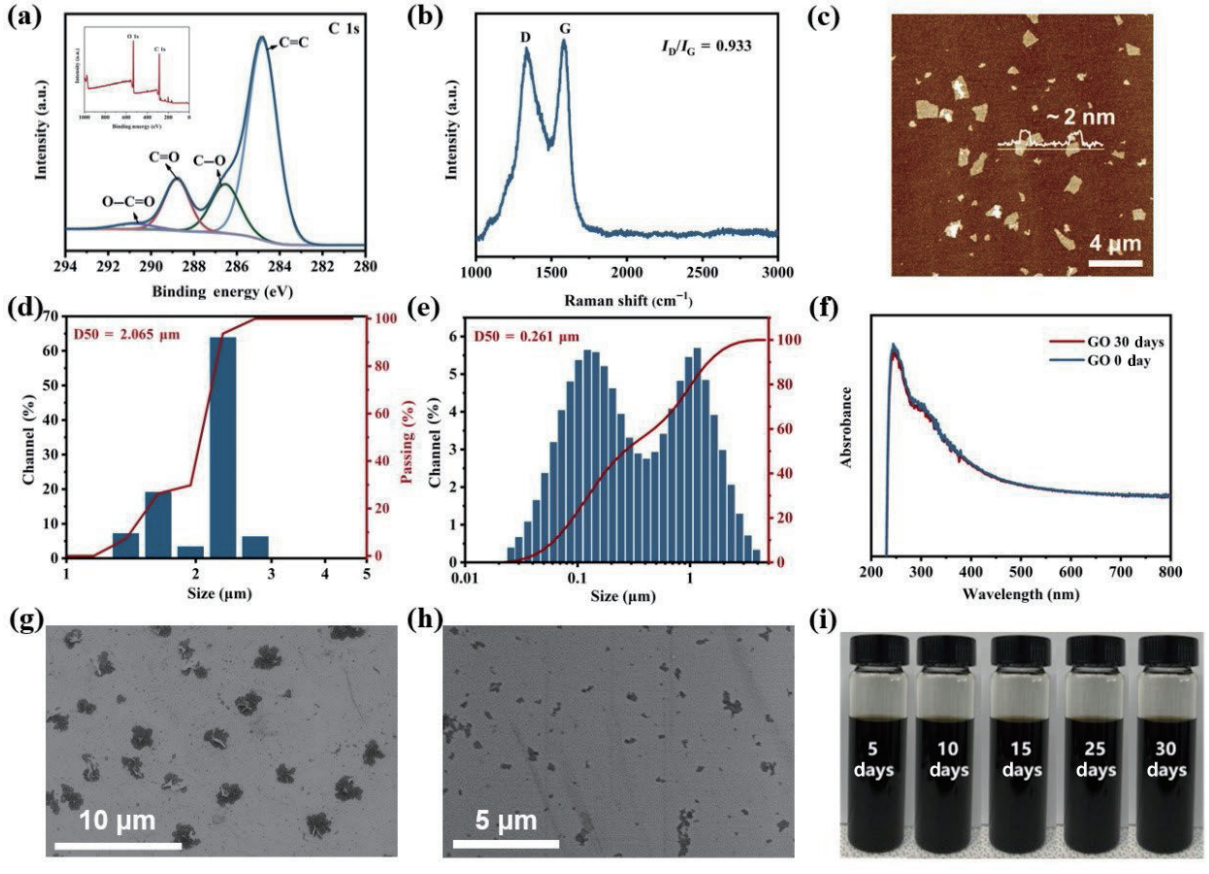

Figure 2 Preparation and characterization of GO dispersion. (a) XPS spectra of raw GO. (b) Raman spectrum of raw GO. (c) AFM image of raw GO. (d) Lateral size distributions of raw GO. (e) Lateral size distributions of GO after processing. (f) UV–vis absorption spectra of GO after processing. (g) SEM image of GO after processing. (h) SEM image of GO after processing. (i) Digital images of GO dispersed in DMAc.

defects and sp^2-bonded graphitic carbon, respectively. The intensity ratio of the D band to G band (I_D/I_G) of the GO fell from 0.933 to 0.827 after ultrasonic treatment, which indicates that ultrasound caused GO to break at the defect, thus improving the structural integrity of GO (Fig. S1 in the Electronic Supplementary Material (ESM)). The AFM image shows that the thickness of GO is about 2 nm (Fig. 2(c)), corresponding to 2 or 3 layers. The particle size analyzer and the SEM image indicate that the average size of GO sheets was about 2 μm when they were dispersed in DMAc (Figs. 2(d) and 2(g)). After ultrasonic treatment, the size of GO sheets was decreased to ~ 300 nm, and they were uniformly dispersed (Figs. 2(e) and 2(h)). The digital photos of GO dispersion show that there is no aggregation after standing for 30 days (Fig. 2(i)). Besides, the relative concentrations of the GO dispersion were further quantitatively characterized by the UV–vis spectra, which did not decline after 30 days, indicating good dispersibility of GO in DMAc for a long time (Fig. 2(f)).

3.2 Tensile properties and characterization of F3-Cl-GO

Figure 3(a) shows the SEM images of F3, F3-Cl, and F3-Cl-GO. Compared with F3, there are obviously more grooves on the surface of F3-Cl, which may be due to the cross-linking reaction between polymer chains during the fiber hot drawing and the elimination of chlorine leaving grooves in the surface of the fibers [47, 48]. Almost no noticeable groove on the surface of F3-Cl-GO means no exposure of highly oriented fibril in the surface of the fiber, indicating the more compact structure of F3-Cl-GO. The TEM image of the axial cross-section of F3-Cl-GO (Fig. 3(b)) shows that GO is evenly dispersed in F3-Cl-GO, and the selected area electron diffraction (SAED) pattern shows obvious lattice spacing of GO (6.77 Å). Besides, the spinning dopes of F3-Cl-GO with different content of GO were characterized by an optical microscope. No agglomeration of GO was found at a lower content of GO, but obvious agglomeration was found when the content was increased to 0.5 wt.% (Fig. S2 in the ESM). Considering that poor dispersion of GO will lead to stress concentration and affect the tensile strength of F3 fibers, 0.3 wt.% of GO was selected as the best addition amount in this work (Fig. S3(a) in the ESM). Figure 3(c) displays that the random fold structure in GO was greatly eliminated through multiple stretches during the spinning process, which laid the foundation for GO to induce the enhancement of polymer chains crystallization and orientation degree.

As we all know, the tensile strength of the fibers is related to their crystallinity and orientation structures. 2D-wide-angle X-ray scattering (WAXS) characterization of F3, F3-Cl, and F3-Cl-GO was performed and the results are shown in Figs. 3(d)–3(f). For F3-Cl, the equatorial diffraction widening can be observed obviously, because the introduction of DABA-Cl with a branched chain structure disrupts the order of the polymer chains. Compared with F3 and F3-Cl, the bright spots of F3-Cl-GO near the equator are more concentrated, indicating that the introduction of GO made the arrangement of polymer chains more orderly. The crystallinity of the fibers was analyzed by one-dimensional (1D)-WAXS (Fig. S3(b) in the ESM), which showed a main peak at $2\theta \approx 9°$. With the introduction of DABA-Cl, the half-peak width of F3-Cl (1.358) becomes wider than F3 (0.911), indicating that

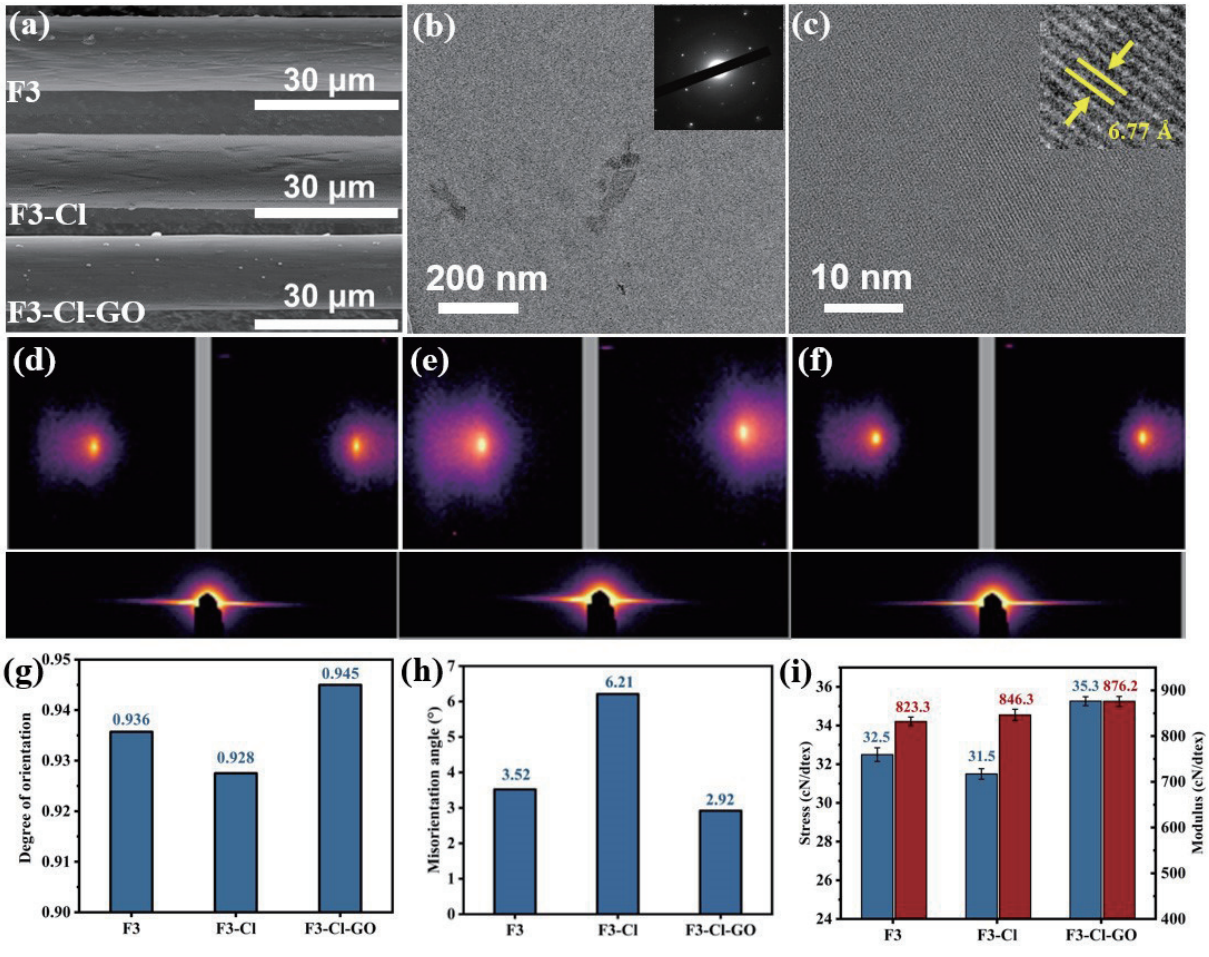

Figure 3 Tensile properties and characterization of composite fibers. (a) SEM images of F3, F3-Cl, and F3-Cl-GO. (b) TEM image of the axial cross-section and SAED analysis of F3-Cl-GO. (c) High-resolution TEM (HRTEM) image of F3-Cl-GO. 2D-WAXS patterns and 2D-SAXS patterns of (d) F3, (e) F3-Cl, and (f) F3-Cl-GO. (g) Degree of orientation of the composite fibers from 2D-WAXS analysis. (h) Microfibril misorientation angle of F3, F3-Cl, and F3-Cl-GO. (i) The strength and modulus of F3, F3-Cl, and F3-Cl-GO.

the crystallinity of the fibers decreased. On this basis, the half-peak width of F3-Cl-GO (0.808) is apparently narrowed, which shows that adding a small amount of GO can promote crystallization (Fig. S3(c) in the ESM). Based on the Hermans equation, the azimuth of the WAXS curve was integrated (Fig. S3(d) in the ESM), and the degree of crystal orientation (f_2) of F3 was calculated. As shown in Fig. 3(g), the f_2 of F3-Cl-GO (0.945) is higher than that of F3 (0.936) and F3-Cl (0.928), which means that the addition of GO is beneficial to improve the orientation degree of macromolecules.

In addition, the orientation misorientation angle of microfibers can be characterized by SAXS (Figs. 3(d)–3(f)). Compared with F3 (3.52) and F3-Cl (6.21), F3-Cl-GO (2.92) shows a lower derived orientation misorientation angle (Fig. 3(h)), which indicates that the arrangement of microfibers in F3-Cl-GO is more ordered. The tensile strength of the fibers is shown in Fig. 3(i) and Table S1 in the ESM. The addition of DABA-Cl caused defects in the fibers and decreased the crystallinity and orientation of the fibers. These reasons resulted in a slight decrease in the tensile strength of F3-Cl (31.5 cN/dtex). The small addition of GO promoted the crystallization and orientation degree of F3-Cl-GO, and higher tensile strength of F3-Cl-GO (35.3 cN/dtex) was obtained.

3.3 Interfacial shear performance and characterization of F3-Cl-GO

The microstructure of the fibers was investigated to determine the effects of DABA-Cl and GO on the IFSS of HAFs. Attenuated total reflection (ATR)-FTIR in the range of 4000–400 cm^{-1} was carefully studied to explore the changes in the aggregation structure of F3 (Fig. 4(a)). It can be found that band II mainly corresponds to –NH– involved in hydrogen bonding interaction in amide groups at ~ 3280 cm^{-1}. It is worth noting that the –NH– wave number of Kevlar 29 is 3320 cm^{-1}, higher than F3-Cl-GO, which indicates that the hydrogen bond interaction in F3-Cl-GO was significantly enhanced. The peak intensity of band II for F3-Cl-GO is higher than that for F3 and F3-Cl, which indicates that the number of hydrogen bonds between the polymer chains of F3-Cl-GO increased, thus increasing the lateral interaction of polymer chains. The vibration absorption peak of C–Cl can also be obviously observed at 1050 cm^{-1}, which confirms the successful synthesis of F3-Cl and F3-Cl-GO, and the existence of Cl can also be confirmed through the XPS spectrum (Fig. S4(a) in the ESM).

Figure 4(b) shows the water contact angle and surface energy of the aramid fibers. With the introduction of DABA-Cl and GO, the

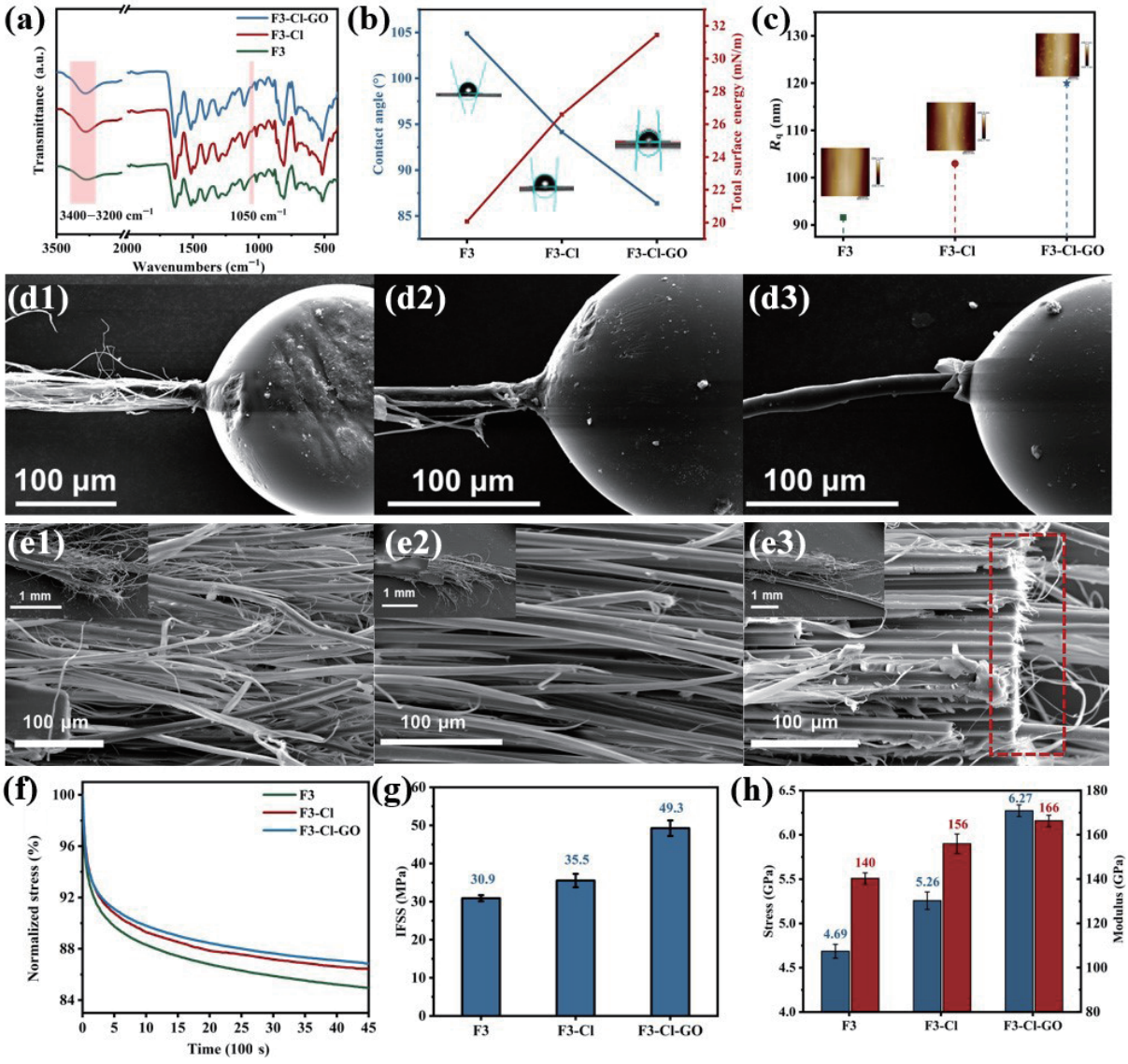

Figure 4 Interfacial shear properties and characterization of composite fibers. (a) FTIR absorption spectra of F3, F3-Cl, and F3-Cl-GO. (b) Contact angle and total surface energy of F3, F3-Cl, and F3-Cl-GO. (c) Roughness of F3, F3-Cl, and F3-Cl-GO. (d) SEM images of F3, F3-Cl, and F3-Cl-GO after pull-out tests. (e) Fracture morphology of F3, F3-Cl, and F3-Cl-GO. (f) Stress relaxation curves of F3, F3-Cl, and F3-Cl-GO. (g) IFSS of F3, F3-Cl, and F3-Cl-GO. (h) Strength and modulus of impregnated fibers.

contact angle decreased from 104.88° to 86.38°, and the surface energy increased from 20.07 to 31.45 mN/m. The results indicate that the introduction of GO and DABA-Cl improved the polarity of fiber surface. It should be noted that the fiber was hot drawn at 400 °C in N_2 atmosphere. In order to explore the stability of oxygen functional group, GO treated at 400 °C in N_2 atmosphere for one minute was characterized by FTIR spectrum and XPS spectrum (Figs. S4(b) and S4(c)). It was found that the O/C decreased from 35% to 30% after heat treatment, but most functional groups remained. This means that GO can still form a large number of hydrogen bonds with polymer chains, thus improving the IFSS of fibers. The surface morphology of F3, F3-Cl, and F3-Cl-GO was characterized by AFM. As shown in Fig. 4(c), root mean square (RMS) roughness (R_q) of F3, F3-Cl, and F3-Cl-GO was 91.6, 109, and 123 nm, respectively. The three-dimensional (3D) image of the fiber surface shows the increase of roughness more clearly (Fig. S5 in the ESM). The increase of the polarity and roughness of the fiber surface further strengthened the adhesive force between fiber and epoxy, thus improving the interfacial shear property of the fibers. In order to ensure the results, five areas of each fiber are selected for testing, and the detailed data are shown in Table S2 in the ESM.

The fibers morphology was characterized by SEM after IFSS testing (Fig. 4(d) and Fig. S6 in the ESM). Fibrillation was observed in both F3 and F3-Cl, and the interface failure was owing to the weak cohesive force between skin and core. However, F3-Cl-GO showed the debonding between fiber and epoxy, with the fiber structure remaining, which indicated that the interaction between polymer chains was significantly enhanced. Furthermore, the interfacial strength of polymer chains was characterized by stress relaxation experiment. The results show that the initial stress retention rate of F3-Cl-GO was higher than those of F3 and F3-Cl (Fig. 4(f)), meaning the higher resistance to interchain slipping of F3-Cl-GO. Due to the introduction of GO, more hydrogen bond is formed between polymer chains. In addition, three kinds of aramid fibers were put into the DMSO-KOH system for swelling (Fig. S7(a) in the ESM). After 20 min, it was found that F3 was totally swollen, but parts of F3-Cl and F3-Cl-GO kept unswollen. Thereinto, the integrity of F3-Cl-GO was obviously higher than that of F3-Cl, which is consistent with previous results. The IFSS of F3, F3-Cl, and F3-Cl-GO is 30.9, 35.5, and 49.3 MPa, respectively. Compared with F3, the strength of IFSS of F3-Cl-GO is increased by 59% (Fig. 4(g) and Fig. S7(b) in the ESM). Detailed data of IFSS can be found in Table S3 in the ESM. Moreover, another comparison of IFSS test between F3 and F3-GO was conducted (Fig. S7(c) in the ESM), and the result shows that the interfacial shear property improvement of F3-GO (37.8 MPa) was not as significant as F3-Cl-GO (49.3 MPa), which confirms the necessity of introducing both GO and DABA-Cl in the system.

In order to further evaluate the tensile property of composites, the impregnated fibers were prepared. According to the fracture morphology analysis of the impregnated fibers (Fig. 4(e)), it is found that the fracture modes of the fibers changed. The fracture of F3 had little resin remaining on the fiber with severe fibrillation phenomenon. In sharp contrast, the interface between F3-Cl-GO and epoxy was intact and the fibrillation phenomenon was reduced after fiber failure, indicating strong lateral force and strong binding force of F3-Cl-GO with epoxy. The tensile strength of the impregnated fibers of F3, F3-Cl, and F3-Cl-GO is 4.69, 5.26, and 6.27 GPa, respectively (Fig. 4(h)), which represents a significant property improvement of 33.7%. In addition, compared with other commercial high-properties fibers (Fig. S7(d) in the ESM), the fibers in this work exhibit better mechanical properties, showing broader industrial prospects.

3.4 Atomistic simulations

To understand the influence of GO on the mechanical behaviors of the fibers, atomistic simulations and relevant analyses were conducted. Our calculations demonstrate the strong binding energy between F3-Cl chains and GO (Fig. 5(a)), indicating that the addition of GO can effectively increase the interfacial interaction for inter-chain stress transfer. Furthermore, tensile tests on F3-Cl and F3-Cl-GO assemblies were performed (Figs. 5(b) and 5(c)). Stress–strain curves (Fig. 5(b)) demonstrate the mechanical enhancement induced by the addition of GO sheets. During the stretching process of F3-Cl assemblies, elastic deformation initially occurs, followed by the crack nucleation and

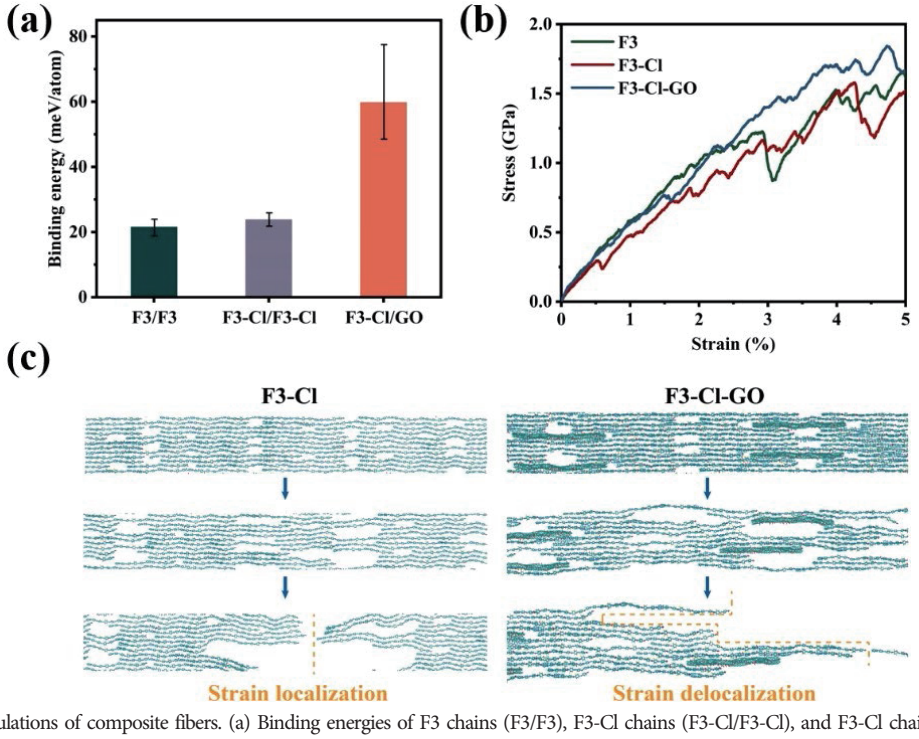

Figure 5 Atomistic simulations of composite fibers. (a) Binding energies of F3 chains (F3/F3), F3-Cl chains (F3-Cl/F3-Cl), and F3-Cl chain onto a GO sheet (F3-Cl/GO). (b) Stress–strain curves of F3, F3-Cl, and F3-Cl-GO assemblies. (c) Simulation snapshots of F3-Cl and F3-Cl-GO assemblies under tension.

propagation from the weakest link (Fig. 5(c)), resulting in strain localizations and failure. This is because the poor interfacial interaction between polymer chains cannot suppress the crack propagation. In contrast to F3-Cl assemblies, F3-Cl-GO assemblies exhibit the strain delocalization. This is because GO sheets bridge adjacent polymer chains and suppress crack propagation since GO sheets have a high specific surface area and strong interfacial interaction with polymer chains (Fig. 5(a)). These analyses account for the enhanced mechanical performance of F3-Cl-GO fibers.

4 Conclusions

In summary, a novel F3-Cl-GO with excellent tensile strength (6.27 GPa) and interfacial shear strength (49.3 MPa) was prepared by *in-situ* polymerization and wet spinning. The introduction of DABZ-Cl increased the surface polarity and roughness of F3, which contributes to the improvement of the interfacial shear property of F3. On this basis, the introduction of GO further promoted the IFSS by increasing the interaction between polymer chains. Moreover, the introduction of GO also enhanced the crystallization and orientation degree of the fibers, which not only made up for the tensile strength deficiency of F3-Cl but also far exceeded the tensile strength of F3. The successful synthesis of F3-Cl-GO will expand a broad application prospect in the field of aramid fiber composites.

Acknowledgements

This work was financially supported by the Ministry of Science and Technology of China (No. 2016YFA0200100), the Beijing National Laboratory for Molecular Sciences (No. BNLMS-CXTD-202001), the National Natural Science Foundation of China (Nos. 52102035, 52021006, T2188101, 51720105003, and 21790052), and the Strategic Priority Research Program of CAS (No. XDB36030100).

Electronic Supplementary Material: Supplementary material (Raman spectra of GO after processing, opticalmicroscopy (OM) images of the spinning dope, tensile strength of the composite fiber, WAXD measurements, XPS spectra of composite fiber, FTIR measurements, AFM photographs for composite fiber surface, physical diagram of composite fiber dissolved in DMSO-KOH, mechanical curve of IFSS measurements, and schematic diagram of IFSS) is available in the online version of this article at https://doi.org/10.1007/s12274-023-5904-7.

References

[1] Li, J. Q.; Wen, Y. Y.; Xiao, Z. H.; Wang, S. J.; Zhong, L. X.; Li, T.; Jiao, K.; Li, L. Y.; Luo, J. J.; Gao, Z. F. et al. Holey reduced graphene oxide scaffolded heterocyclic aramid fibers with enhanced mechanical performance. *Adv. Funct. Mater.* **2022**, *32*, 2200937.

[2] Kim, H. C.; Sodano, H. A. Ultra-high toughness fibers using controlled disorder of assembled aramid nanofibers. *Adv. Funct. Mater.* **2022**, *33*, 2208661.

[3] Zhao, Y.; Li, X.; Shen, J. N.; Gao, C. J.; Van Der Bruggen, B. The potential of Kevlar aramid nanofiber composite membranes. *J. Mater. Chem. A* **2020**, *8*, 7548–7568.

[4] Xie, C. J.; Guo, Z. X.; Qiu, T.; Tuo, X. L. Construction of aramid engineering materials via polymerization-induced *para*-aramid nanofiber hydrogel. *Adv. Mater.* **2021**, *33*, 2101280.

[5] Zhou, J. Y.; Thaiboonrod, S.; Fang, J. H.; Cao, S. M.; Miao, M.; Feng, X. *In-situ* growth of polypyrrole on aramid nanofibers for electromagnetic interference shielding films with high stability. *Nano Res.* **2022**, *15*, 8536–8545.

[6] Chen, F. X.; Zhai, L. S.; Yang, H. Y.; Zhao, S. C.; Wang, Z. L.; Gao, C.; Zhou, J. Y.; Liu, X.; Yu, Z. W.; Qin, Y. et al. Unparalleled armour for aramid fiber with excellent UV resistance in extreme environment. *Adv. Sci.* **2021**, *8*, 2004171.

[7] Wang, H. M.; Wang, H. M.; Wang, Y. L.; Su, X. Y.; Wang, C. Y.; Zhang, M. C.; Jian, M. Q.; Xia, K. L.; Liang, X. P.; Lu, H. J. et al. Laser writing of janus graphene/kevlar textile for intelligent protective clothing. *ACS Nano* **2020**, *14*, 3219–3226.

[8] Yang, B.; Wang, L.; Zhang, M. Y.; Luo, J. J.; Lu, Z. Q.; Ding, X. Y. Fabrication, applications, and prospects of aramid nanofiber. *Adv. Funct. Mater.* **2020**, *30*, 2000186.

[9] Su, L. Y.; Ma, X. Y.; Zhou, J. L.; Liu, X. C.; Du, F. L.; Teng, C. Large-scale preparation of high-performance boron nitride/aramid nanofiber dielectric composites. *Nano Res.* **2022**, *15*, 8648–8655.

[10] Zuo, X. W.; Fan, T. T.; Qu, L. J.; Zhang, X. J.; Miao, J. L. Smart multi-responsive aramid aerogel fiber enabled self-powered fabrics. *Nano Energy* **2022**, *101*, 107559.

[11] Yin, L. J.; Zhang, B.; Tian, M.; Ning, N. Y.; Zhang, L. Q.; Wang, W. C. Surface construction of ANF/CNT onto aramid fibers to enhance interfacial adhesion and provide real-time monitoring of deformation. *Compos. Sci. Technol.* **2022**, *223*, 109336.

[12] Yuan, Y. H.; Dai, Y.; Meng, C. B.; Luo, L. B.; Liu, X. Y. Improving compressive strength of aramid fiber by introducing carbon nanotube derivates grafted with oligomers of different conformations and controlling its alignment. *Macromol. Mater. Eng.* **2019**, *304*, 1900127.

[13] Nasser, J.; Zhang, L. S.; Lin, J. J.; Sodano, H. Aramid nanofiber reinforced polymer nanocomposites via amide–amide hydrogen bonding. *ACS Appl. Polym. Mater.* **2020**, *2*, 2934–2945.

[14] Nam, K. H.; Yu, J.; You, N. H.; Han, H.; Ku, B. C. Synergistic toughening of polymer nanocomposites by hydrogen-bond assisted three-dimensional network of functionalized graphene oxide and carbon nanotubes. *Compos. Sci. Technol.* **2017**, *149*, 228–234.

[15] Cheng, Z.; Zhang, L. J.; Jiang, C.; Dai, Y.; Meng, C. B.; Luo, L. B.; Liu, X. Y. Aramid fiber with excellent interfacial properties suitable for resin composite in a wide polarity range. *Chem. Eng. J.* **2018**, *347*, 483–492.

[16] Stockdale, T. A.; Cole, D. P.; Staniszewski, J. M.; Roenbeck, M. R.; Papkov, D.; Lustig, S. R.; Dzenis, Y. A.; Strawhecker, K. E. Hierarchical mechanisms of lateral interactions in high-performance fibers. *ACS Appl. Mater. Interfaces* **2020**, *12*, 22256–22267.

[17] Cheng, Z.; Liu, Y.; Meng, C. B.; Dai, Y.; Luo, L. B.; Liu, X. Y. Constructing a weaving structure for aramid fiber by carbon nanotube-based network to simultaneously improve composites interfacial properties and compressive properties. *Compos. Sci. Technol.* **2019**, *182*, 107721.

[18] Yang, Y.; Min, C.; Xu, Z.; Liang, H.; Li, Q.; Ji, M.; Liu, S.; Wang, W.; Li, N.; Pei, X. Strong interfacial modified aramid fabric reinforced degradable thermosetting composites: Reinforcing and tribological effects. *Mater. Today Chem.* **2022**, *24*, 100795.

[19] Gong, X. Y.; Liu, Y. Y.; Huang, M. N.; Dong, Q. L.; Naik, N.; Guo, Z. H. Dopamine-modified aramid fibers reinforced epoxidized natural rubber nanocomposites. *Compos. Commun.* **2022**, *29*, 100996.

[20] Zhang, Y. H.; Huang, Y. D.; Liu, L.; Cai, K. L. Effects of γ-ray radiation grafting on aramid fibers and its composites. *Appl. Surf. Sci.* **2008**, *254*, 3153–3161.

[21] Xing, L. X.; Liu, L.; He, M.; Wu, Z. J.; Huang, Y. D. Effect of different graft polymerization systems on surface modification of aramid fibers with Γ-ray radiation. *Adv. Mater. Res.* **2013**, *658*, 80–84.

[22] Wang, J.; Chen, P.; Li, H.; Zhang, C. S.; Sun, B. L.; Zhang, X. Y. The analysis of Armos fibers reinforced poly(phthalazinone ether sulfone ketone) composite surfaces after oxygen plasma treatment. *Surf. Coat. Technol.* **2008**, *202*, 4986–4991.

[23] Nasser, J.; Lin, J. J.; Steinke, K.; Sodano, H. A. Enhanced interfacial strength of aramid fiber reinforced composites through adsorbed aramid nanofiber coatings. *Compos. Sci. Technol.* **2019**, *174*, 125–133.

[24] Chakraborty, D.; Saha, S.; Dey, S.; Pramanik, S. Enhanced mechanical toughness of carbon nanofibrous-coated surface modified Kevlar reinforced polyurethane/epoxy matrix hybrid composites. *J. Appl. Polym. Sci.* **2020**, *137*, 48802.

[25] Ehlert, G. J.; Lin, Y. R.; Sodano, H. A. Carboxyl functionalization of carbon fibers through a grafting reaction that preserves fiber tensile strength. *Carbon* **2011**, *49*, 4246–4255.

[26] Gao, B.; Zhang, R. L.; Gao, F. C.; He, M. S.; Wang, C. G.; Liu, L.; Zhao, L. F.; Cui, H. Z. Interfacial microstructure and enhanced mechanical properties of carbon fiber composites caused by growing generation 1–4 dendritic poly(amidoamine) on a fiber surface. *Langmuir* **2016**, *32*, 8339–8349.

[27] Zhang, L. W.; Kong, H. J.; Qiao, M. M.; Ding, X. M.; Yu, M. H. Growing nano-SiO_2 on the surface of aramid fibers assisted by supercritical CO_2 to enhance the thermal stability, interfacial shear strength, and UV resistance. *Polymers* **2019**, *11*, 1397.

[28] Lv, J. W.; Cheng, Z.; Wu, H.; He, T. J.; Qin, J. Q.; Liu, X. Y. *In-situ* polymerization and covalent modification on aramid fiber surface via direct fluorination for interfacial enhancement. *Compos. Part B: Eng.* **2020**, *182*, 107608.

[29] Wang, L.; Shi, Y. X.; Chen, S. X.; Wang, W. C.; Tian, M.; Ning, N. Y.; Zhang, L. Q. Highly efficient mussel-like inspired modification of aramid fibers by UV-accelerated catechol/polyamine deposition followed chemical grafting for high-performance polymer composites. *Chem. Eng. J.* **2017**, *314*, 583–593.

[30] Dai, Y.; Han, Y. T.; Yuan, Y. H.; Meng, C. B.; Cheng, Z.; Luo, L. B.; Qin, J. Q.; Liu, X. Y. Synthesis of heterocyclic aramid fiber based on solid-phase cross-linking of oligomers with reactive end group. *Macromol. Mater. Eng.* **2018**, *303*, 1800076.

[31] Dai, Y.; Yuan, Y. H.; Luo, L. B.; Liu, X. Y. A facile strategy for fabricating aramid fiber with simultaneously high compressive strength and high interfacial shear strength through cross-linking promoted by oxygen. *Compos. Part A:Appl. Sci. Manuf.* **2018**, *113*, 233–241.

[32] Wen, F.; Zhu, C. L.; Li, L. L.; Zhou, B.; Zhang, L.; Han, C.; Li, W. J.; Yue, Z. J.; Wu, W.; Wang, G. F. et al. Enhanced energy storage performance of polymer nanocomposites using hybrid 2D ZnO@MoS_2 semiconductive nano-fillers. *Chem. Eng. J.* **2022**, *430*, 132676.

[33] Mechin, P. Y.; Keryvin, V.; Grandidier, J. C. Effect of the nano-filler content on the compressive strength of continuous carbon fibre/epoxy matrix composites. *Compos. Part B:Eng.* **2021**, *224*, 109223.

[34] Luo, J. J.; Wen, Y. Y.; Jia, X. Z.; Lei, X. D.; Gao, Z. F.; Jian, M. Q.; Xiao, Z. H.; Li, L. Y.; Zhang, J. W.; Li, T. et al. Fabricating strong and tough aramid fibers by small addition of carbon nanotubes. *Nat. Commun.* **2023**, *14*, 3019.

[35] Palermo, V.; Kinloch, I. A.; Ligi, S.; Pugno, N. M. Nanoscale mechanics of graphene and graphene oxide in composites: A scientific and technological perspective. *Adv. Mater.* **2016**, *28*, 6232–6238.

[36] Kinloch, I. A.; Suhr, J.; Lou, J.; Young, R. J.; Ajayan, P. M. Composites with carbon nanotubes and graphene: An outlook. *Science* **2018**, *362*, 547–553.

[37] Gong, L.; Young, R. J.; Kinloch, I. A.; Riaz, I.; Jalil, R.; Novoselov, K. S. Optimizing the reinforcement of polymer-based nanocomposites by graphene. *ACS Nano* **2012**, *6*, 2086–2095.

[38] Kim, J.; Kim, J.; Song, S.; Zhang, S. Y.; Cha, J.; Kim, K.; Yoon, H.; Jung, Y.; Paik, K. W.; Jeon, S. Strength dependence of epoxy composites on the average filler size of non-oxidized graphene flake. *Carbon* **2017**, *113*, 379–386.

[39] Gao, Z.; Zhu, J. D.; Rajabpour, S.; Joshi, K.; Kowalik, M.; Croom, B.; Schwab, Y.; Zhang, L. W.; Bumgardner, C.; Brown, K. R. et al. Graphene reinforced carbon fibers. *Sci. Adv.* **2020**, *6*, eaaz4191.

[40] Zhou, H.; Jiao, K. Carbonene materials modified high-performance polymer fibers: Preparation, properties, and applications. *Acta Phys. Chim. Sin.* **2022**, *38*, 2111041.

[41] Li, T. J.; Meng, Z. X.; Keten, S. Interfacial mechanics and viscoelastic properties of patchy graphene oxide reinforced nanocomposites. *Carbon* **2020**, *158*, 303–313.

[42] Paredes, J. I.; Villar-Rodil, S.; Martínez-Alonso, A.; Tascón, J. M. D. Graphene oxide dispersions in organic solvents. *Langmuir* **2008**, *24*, 10560–10564.

[43] Wang, G. R.; Liu, L. Q.; Zhang, Z. Interface mechanics in carbon nanomaterials-based nanocomposites. *Compos. Part A:Appl. Sci. Manuf.* **2021**, *141*, 106212.

[44] Ramanathan, T.; Abdala, A. A.; Stankovich, S.; Dikin, D. A.; Herrera-Alonso, M.; Piner, R. D.; Adamson, D. H.; Schniepp, H. C.; Chen, X.; Ruoff, R. S. et al. Functionalized graphene sheets for polymer nanocomposites. *Nat. Nanotechnol.* **2008**, *3*, 327–331.

[45] Ming, X.; Wei, A. R.; Liu, Y. J.; Peng, L.; Li, P.; Wang, J. Q.; Liu, S. P.; Fang, W. Z.; Wang, Z. Q.; Peng, H. Q. et al. 2D-topology-seeded graphitization for highly thermally conductive carbon fibers. *Adv. Mater.* **2022**, *34*, 2201867.

[46] Qiu, B. W.; Sun, T.; Yuan, M. S.; Zhang, H. R.; Chen, Y.; Zhou, S. T.; Heng, Z. G.; Liang, M.; Zou, H. W. Effect of different lateral dimension graphene oxide sheets on the interface of carbon fiber reinforced polymer composites. *Compos. Sci. Technol.* **2021**, *213*, 108939.

[47] Luo, L. B.; Yuan, Y. H.; Dai, Y.; Cheng, Z.; Wang, X.; Liu, X. Y. The novel high performance aramid fibers containing benzimidazole moieties and chloride substitutions. *Mater. Des.* **2018**, *158*, 127–135.

[48] Sweeny, W. Improvements in compressive properties of high modulus fibers by crosslinking. *J. Polym. Sci. Part A Polym. Chem.* **1992**, *30*, 1111–1122.

Electronic Supplementary Material

Simultaneously enhanced interfacial shear strength and tensile strength of heterocyclic aramid fiber by graphene oxide

Ziyi Zhang[1,2,3], Xiangzheng Jia[4], Chun Li[3], Lanying Li[5], Yeye Wen[2], Zhenfei Gao[3], Jiangwei Zhang[6], Enlai Gao[4] (✉), Kun Jiao[2,3] (✉), and Jin Zhang[2,3] (✉)

[1] *College of Science, China University of Petroleum (Beijing), Beijing 102249, China*
[2] *Beijing National Laboratory for Molecular Sciences, School of Materials Science and Engineering, College of Chemistry and Molecular Engineering, Beijing Science and Engineering Center for Nanocarbons, Peking University, Beijing 100871, China*
[3] *Beijing Graphene Institute (BGI), Beijing 100095, China*
[4] *Department of Engineering Mechanics, School of Civil Engineering, Wuhan University, Wuhan 430072, China*
[5] *China Bluestar Chengrand Chemical Co., Ltd., Chengdu 610041, China*
[6] *Science Center of Energy Material and Chemistry, College of Chemistry and Chemical Engineering, Inner Mongolia University, Hohhot 010021, China*

Supporting information to https://doi.org/10.1007/s12274-023-5904-7

Address correspondence to Enlai Gao, enlaigao@whu.edu.cn; Kun Jiao, jiaokun-cnc@pku.edu.cn; Jin Zhang, jinzhang@pku.edu.cn

EXPERIMENTAL METHODS

Mechanism properties evaluation

Fiber mechanical properties test: Firstly, the fiber is twisted on a twisting machine, and the twisting twist formula is as follows: TPM= (1055±50)/$\sqrt{T}$, where TPM represents twisting twist required by the fiber, T is the measured fiber line density. The fiber is placed on the tension machine to ensure that the fiber bundle is axially stretched in the middle of the two fixtures, and the pre-tension is applied. The clamp spacing was (170±1) mm and the tensile speed was (25.4±0.1) mm/min.

Fiber impregnation performance test : Before the test, the fiber should be impregnated for preparation. Epoxy resin A, curing agent of epoxy resin A and acetone were used as impregnation raw materials, and their weights were 100 g, 27 g and 21.6 g respectively. The curing agent is first dissolved in acetone, and then compounded with epoxy resin A to prepare the adhesive solution. Pour the prepared glue liquid into the glue tank, and control the temperature of the glue liquid within the range of 23 °C ~ 38 °C. After pouring the glue into the dipping tank, the compound silk is introduced into the glue tank through the yarn guide, tension controller and regulating wheel, and the excess glue is removed by scraping sponge. Then the fiber is wound around the winding sample frame. The impregnated fiber was left at room temperature for 20 h, then dried in an oven at 90 °C for 2 h and at 150 °C for 3 h to cure the resin. After impregnation, the fiber weight is recorded as G_1, and the length is recorded as L_1. The length of the unimpregnated fiber is L_2, and its weight is G_2. Sample glue content Wg follows the formula: $Wg = 100\% \times (G_2/L_2 - G_1/L_1)/(G_1/L_1)$ control glue content of 50%-55%. The mechanical properties of the impregnated fiber are also obtained by uniaxial tensile test with a tensile rate of 10 mm min^{-1}. The sample was fixed on the cardboard frame with epoxy resin before testing, and the test length of the sample was 250 mm.

Interfacial shear strength test: Based on UTM150 micro-nano tensile system, a microdrop embedding and pulling out experiment was designed for heterocyclic aramid fibers system in this paper, and the interfacial shear strength of the fiber was tested. Assuming that the microdroplet is spherical and uniformly around the fiber surface, and the interfacial shear stress is evenly

distributed, the interfacial shear strength can be calculated by $\varepsilon=F/\pi DL$, where F is the droplet pulling load, D is the fiber diameter, and L is the droplet coating length. When preparing the sample, the fiber to be tested should be randomly selected first. The surface of the fiber should be smooth and complete. The fiber is fixed on the rigid sample frame by epoxy resin, and the fiber length is 2 cm (Figure S6a). Epoxy E51 resin was used as the droplet solution for embedding, and D230 polyether amine was used as the curing agent. The mass ratio of the two was 3:1. The evenly mixed solution was placed in a 100 °C incubator for 8 min to control its viscosity. Take out the resin solution, dip a small amount of resin with the tip of a needle and transfer it to the surface of the fiber to be measured. The size of the resin droplet can be adjusted by the thickness of the needle. After curing at room temperature for 24 h, the sample for microdroplet extraction was prepared.

During the test, the lower end of the rigid frame used to hold the fiber sample is fixed to the lower end of the instrument fixture attached to the sensor (Figure S6a). The upper fixture of the instrument is replaced with a self-made stainless steel clamping chuck, and the clamping groove of the stainless-steel clamping chuck is placed under the droplet. As the chuck moves upward, the slot approaches the microdroplet and contacts it, eventually scraping the microdroplet away from the fiber surface (Figure S6b). The load is recorded using a sensor to which the chuck is linked.

Atomistic calculations

Atomistic simulations were performed using the polymer consistent force field (PCFF) to describe the interatomic potentials[1, 2]. All simulations were conducted using large-scale atomic/molecular massively parallel simulator (LAMMPS) computational package[3]. The long-range Columbia interaction was included using particle-particle-particle mesh (PPPM) method[4], while the van der Waals interaction was described by the 9-6 Lennard-Jones potential $\varepsilon[2(\sigma/r)^9 - 3(\sigma/r)^6]$ with a cutoff distance of 1.0 nm.

To calculate the binding energies, the models of F3 chains (F3/F3), F3-Cl chains (F3-Cl/F3-Cl), and F3-Cl chain onto a GO sheet (F3-Cl/GO) were constructed. The binding energy for each model was calculated as the sum of the energies of the isolated chains/sheets minus the total energy of the adsorbed structure upon structural optimization (normalized per atom).

To investigate the mechanical behaviors F3-Cl and F3-Cl-GO assemblies, tensile tests were performed. The model of the F3-Cl assembly was formed by arranging F3-Cl chains in a brick-wall manner, while the model of the F3-Cl-GO assembly was formed by additionally inserting GO sheets. To integrate the Newton equations of motion, the Verlet algorithm was adopted with a time step of 0.5 fs. Before the tensile deformation protocol was applied, the constructed structures were energy minimized using a conjugate gradient algorithm. Afterwards, mechanical responses to tensile loads of these structures were investigated at nearly zero Kelvin using a Nosé-Hoover thermostat. Periodic boundary conditions were applied along all directions. The strain rate was set as 10^8 s^{-1}.

EXPERIMENTAL DATA

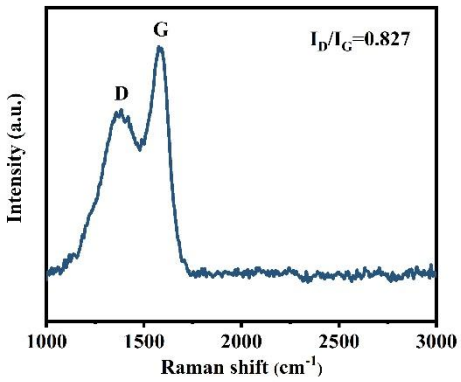

Figure S1 Raman spectra of GO after processing.

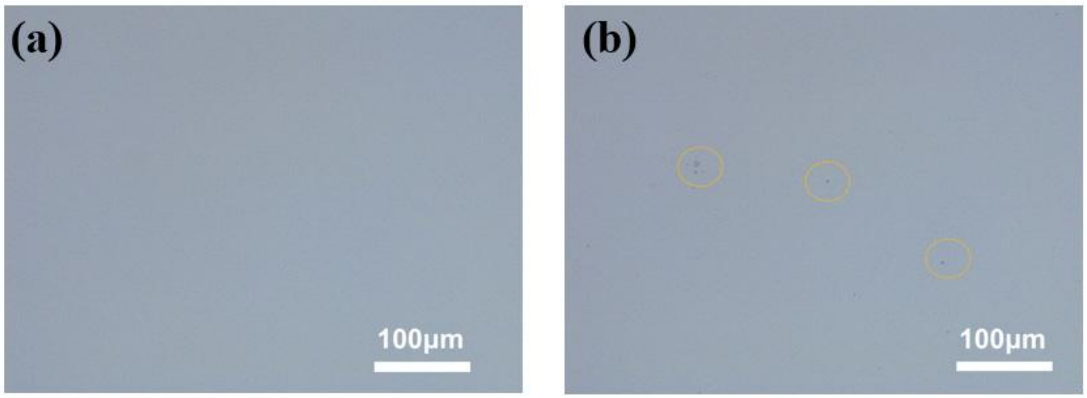

Figure S2 OM images of the spinning dope with different addition contents of GO (a) 0.3 wt%; (b) 0.5 wt%.

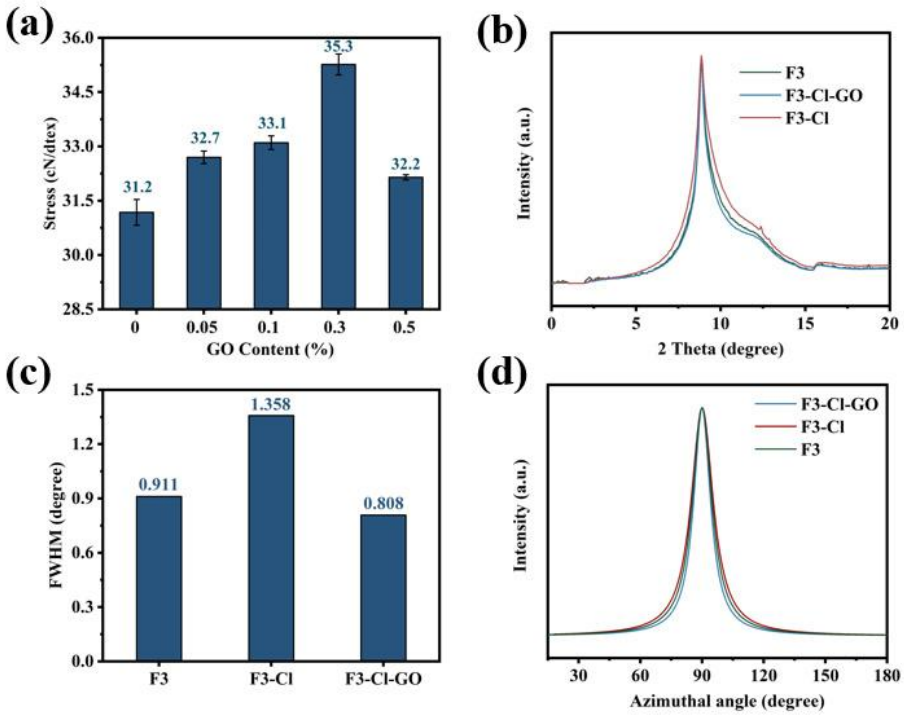

Figure S3 (a) Tensile strength of the composite fiber with different GO concentrations. (b) 1D WAXS profiles of composite fiber. (c) Comparison of the FWHM of composite fiber from the 1D-WAXS curves. (d) Azimuthal intensity profile of composite fiber from the 2D-WAXS analysis.

Table S1 Mechanical properties of three aramid fibers

Samples	Tensile strength (cN/dtex) and Initial modulus (cN/dtex)									
	1		2		3		4		5	
F3	32.8	823.5	32.5	828.3	32.7	844.7	32.6	839.8	31.9.	825.1
F3-Cl	31.5	855.3	31.8	825.1	31.7	845.2	31.4	850.5	31.1	855.6
F3-Cl-GO	35.2	860.5	35.3	884.9	34.9	886.4	35.5	870.6	35.4	878.6

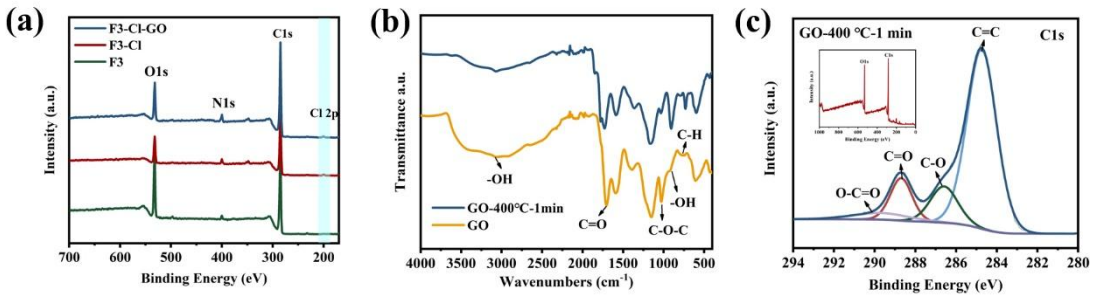

Figure S4 (a) XPS spectra of composite fiber. (b) FTIR spectra of samples GO-400 ℃-1min and GO. (c) XPS spectra of GO-400 ℃-1min.

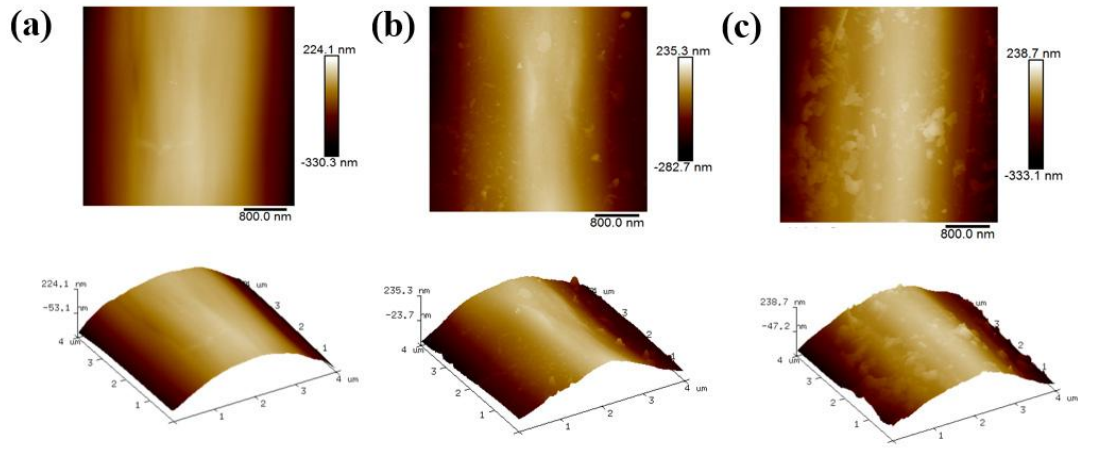

Figure S5 AFM photographs for composite fiber surface (a) F3, (b) F3-Cl, (c) F3-Cl-GO.

Table S2 Surface roughness of composite fibers (4 μm×4 μm)

Samples	Root mean square surface roughness Rq (RMS)/nm				
	area 1	area 2	area 3	area 4	area 5
F3	91.6	91.9	91	88.3	94.4
F3-Cl	100	109	103	107	108
F3-Cl-GO	123	131	116	112	110

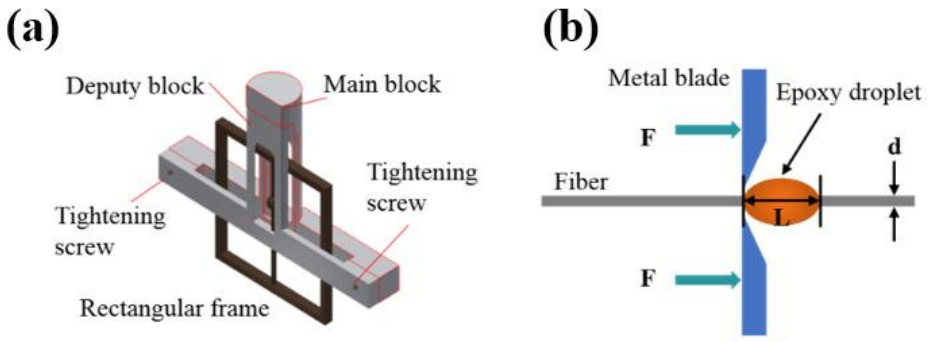

Figure S6 (a) Schematic diagram of droplet removal device. (b) Schematic diagram of microdroplet removal experiment.

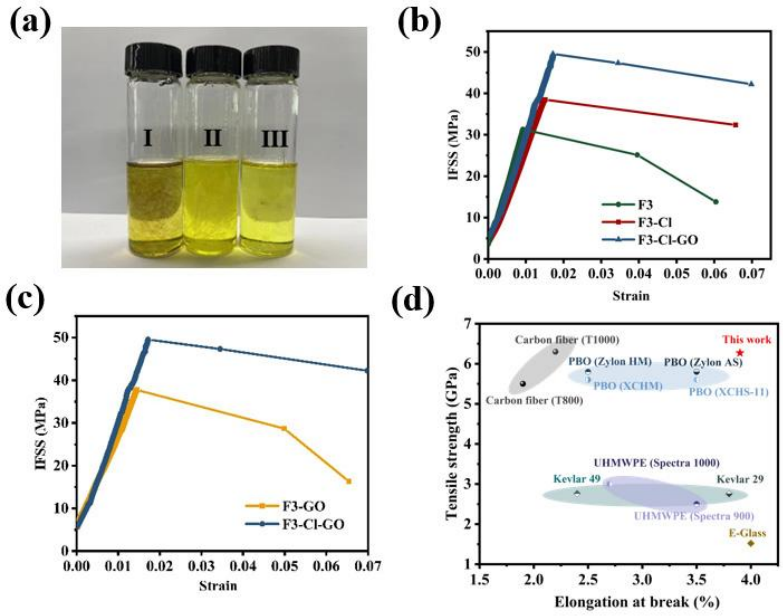

Figure S7 (a) Physical diagram of composite fiber dissolved in DMSO-KOH: (I) F3-Cl-GO, (II) F3-Cl, (III) F3. (b) Mechanical curve of droplet pull-out test for F3, F3-Cl and F3-Cl-GO. (c) Mechanical curve of droplet pull-out test for F3-GO and F3-Cl-GO. (d) Strength and elongation at break of various high-performance fibers.

Table S3 Interfacial shear strength of three aramid fibers

Samples	Interfacial shear strength IFSS (MPa)				
	1	2	3	4	5
F3	31.4	31.2	29.8	30.3	31.7
F3-Cl	35.5	33.4	38.2	35.8	34.7
F3-Cl-GO	46.7	49.7	52.2	49.5	48.2

References

[1] Sun, H.;Mumby, S. J.;Maple, J. R.; Hagler, A. T. An ab Initio CFF93 All-Atom Force Field for Polycarbonates. *J. Am. Chem. Soc.* **1994**, *116*, 2978-2987.

[2] Lordi, V.; Yao, N. Molecular mechanics of binding in carbon-nanotube–polymer composites. *J. Mater. Res.* **2000**, *15*, 2770-2779.

[3] Plimpton, S. Fast Parallel Algorithms for Short-Range Molecular Dynamics. *Journal of Computational Physics* **1995**, *117*, 1-19.

[4] R.W Hockney, J. W. E. *Computer Simulation using Particles*; Taylor & Francis, 1989.